metals

MDPI

Article

Spall Failure of ECAE Mg-Al Alloys at Extreme Strain Rates: Influence of a Refined Precipitate and Grain Microstructure

Christopher S. DiMarco [1,*], Peter Lim [1], Debjoy Mallick [1,2], Laszlo Kecskes [1,3,4], Timothy P. Weihs [1,4] and K. T. Ramesh [1,3,4]

[1] Hopkins Extreme Materials Institute, Johns Hopkins University, 3400 N. Charles Street, Baltimore, MD 21218, USA
[2] DEVCOM Army Research Laboratory, Aberdeen Proving Ground, MD 21005, USA
[3] Department of Mechanical Engineering, Johns Hopkins University, 3400 N. Charles Street, Baltimore, MD 21218, USA
[4] Department of Materials Science and Engineering, Johns Hopkins University, 3400 N. Charles Street, Baltimore, MD 21218, USA
* Correspondence: c.dimarco@jhu.edu

Abstract: The development of advanced materials for extreme dynamic environments requires an understanding of the links between the microstructure and the response of the material (i.e., Materials-by-Design). Spall failure significantly limits material performance at high strain rates, but our understanding of the influence of microstructure on spall strength is limited. While models suggest that increasing the static yield strength by adding precipitates or refining grain size can improve the spall strength, it is possible that the associated increase in nucleation sites may have deleterious effects on spall performance. Herein, we examine spall failure of a Magnesium-Aluminum system with precipitation and grain size strengthening through novel high-throughput laser-driven micro-flyer (LDMF) impact experiments. Six microstructures are investigated, four with grain sizes around 2–3 μm and precipitates around 0.5–1 μm, and two that are precipitate-free with grain sizes around 500 μm at six and nine percent Aluminum contents. The LDMF method allows us to detect differences in spall strength with relatively small changes in microstructure. The spall strength is observed to be strongly affected by varying levels of precipitates and consistently shows a notable reduction in average spall strength around 8–19% with the addition of precipitates, with values ranging from 1.22–1.50 GPa. The spall strength is also seen to decrease with the refinement of grain size independent of composition. However, this decrease is small compared to the hundred-fold grain size reduction. While ductile void growth is observed across all samples, greater variability and a further decrease in strength are seen with an increasing numbers of non-uniformly dispersed precipitates.

Keywords: magnesium alloys; Materials-by-Design; severe plastic deformation; equal channel angular extrusion; microstructure; grain size strengthening; precipitation strengthening; high strain rate; laser shock; spall failure; dynamic failure

check for updates

Citation: DiMarco, C.S.; Lim, P.; Mallick, D.; Kecskes, L.; Weihs, T.P.; Ramesh, K.T. Spall Failure of ECAE Mg-Al Alloys at Extreme Strain Rates: Influence of a Refined Precipitate and Grain Microstructure. *Metals* **2023**, *13*, 454. https://doi.org/10.3390/met13030454

Academic Editor: Ruslan R. Balokhonov

Received: 30 January 2023
Revised: 16 February 2023
Accepted: 20 February 2023
Published: 22 February 2023

Copyright: © 2023 by the authors. Licensee MDPI, Basel, Switzerland. This article is an open access article distributed under the terms and conditions of the Creative Commons Attribution (CC BY) license (https://creativecommons.org/licenses/by/4.0/).

1. Introduction

Improvements to advanced materials are required to withstand extreme conditions. Since such environments consist of multiple modes of failure, an understanding of the influence of microstructure on the underlying dynamic failure mechanisms is necessary for Materials-by-Design. In turn, an efficient navigation of the vast landscape of potential materials requires reliable predictive models that are validated by laboratory data.

A major extreme environment of interest is that of high-rate dynamic tension, leading to spall failure [1,2]. Spall failure in metals occurs through the rapid nucleation, unstable growth, and coalescence of voids within the material [3,4]. The nucleation and growth processes are strongly coupled to the microstructure of the metal, and so spall failure should be highly sensitive to microstructure. However, there is little experimental data

on the dependence of spall on microstructure [5–9]. Given the wide range of potential microstructures in metals, the major challenge associated with understanding spall is that of having sufficient experimental data on the influence of microstructure on spall [10,11]. Current spall experiments are expensive and difficult, and so there are very limited datasets that explore the connections between spall and microstructure.

The canonical experiment for exploring the spall failure process is the plate impact experimental configuration using gas gun launchers [12–15]. In such an experiment, the spall failure occurs when two rarefaction waves interact within a material to create a region of rapidly increasing tensile stress [1,2]. Such experiments are expensive and require large samples. In contrast, laser-shock methods feature similar energy densities, but are relatively safe, operate at much smaller scales, require only a table-top set-up, and need far less material per experiment. Laser-shock methods are uniquely poised to facilitate a large number of high-strain-rate experiments [16–21], and enable testing rates of hundreds of tests per day (traditional experiments may permit 1–4 experiments/day). The last few decades have seen the development of Laser-Driven Micro-Flyer (LDMF) experiments, but much of the work has been on shock compression rather than spall failure.

Magnesium and its alloys are of particular interest because of their high strength-to-weight ratio, but they suffer from low dynamic failure strains [22,23]. One idea that is prevalent in the literature is that to improve ductile spall resistance, we must tailor the microstructure to maximize the benefits of increasing yield strength and thus the resistance to void growth, while minimizing the detrimental effects of introducing higher densities of failure nucleation sites [24–27]. Mallick et al. [11], in a compendium developed under the Johns Hopkins University Center for Materials in Extreme Dynamic Environments (CMEDE) program, provide an excellent review of the current state of understanding of spall failure in Mg and Mg alloys. While refined grain structures have been widely investigated, work on understanding the effects of precipitation strengthening on spall is limited [14,25,28–30]. Furthermore, FEM simulations suggest that large precipitates can act as nucleation sites with no improvement in the void growth resistance [30]; thus large precipitates are thought detrimental with respect to the spall failure mechanism.

Informed by these prior results, we hypothesize that increased yield strength without an increased nucleation site density is likely needed to see a meaningful improvement in spall strength. The yield strength can be increased, for example, through solute strengthening, grain boundary strengthening, and precipitate strengthening; however, the precipitates must remain small to avoid additional void nucleation. Therefore, the microstructure goals in this work are to create, within a Mg-Al system: (1) a more refined grain structure, and (2) a more uniformly distributed precipitate structure. We rely on Equal Channel Angular Extrusion (ECAE) to achieve these microstructure goals.

We utilize our recently developed high-throughput LDMF experimental characterization methods [19] to interrogate the role of microstructure in the spall failure of ECAE-processed Mg-Al alloys (these specific materials are considered for reasons described et seq.). We demonstrate high-throughput spall failure characterization at both an unprecedented number (over 500 experiments performed) and at an unprecedented rate of experimentation (up to 30 experiments per hour). We then couple this to optical and scanning electron microscope (SEM) characterization of the spall failure surfaces to understand the fundamental mechanisms at play. Finally, we discuss our key observations and identify some specific insights from the work.

2. Materials and Methods

We examine supersaturated Mg-Al alloys with 6–9% of Al. The supersaturated Mg-Al system produces precipitate structures both within the grains and at grain boundaries. Depending on processing conditions, the precipitates can be highly textured and have widely varying aspect ratios. Control of alloy composition and process conditions through extrusion rate, specimen orientation, and temperature produces a uniform microstructure of finer grains with uniformly distributed isotropic precipitates. The two compositions,

Mg-6Al and Mg-9Al (wt.%), are subjected to two different ECAE processing routes to develop the targeted microstructures. We compare these materials against their as-cast fully-solutionized counterparts.

2.1. ECAE Processing of Mg-Al Alloys

We fabricated a series of two binary Mg-Al alloy plates for the spall experiments in this study. The as-received ingots were received from Dr. Zhigang Xu at North Carolina A&T University, Greensboro, NC. The alloys were synthesized by melting high purity metal precursors together in an argon environment. The melt was first superheated and then the temperature was lowered to cause denser impurities, e.g., Fe, to settle to the bottom of the tundish. Subsequently, the melt was poured through a porous Al_2O_3 filter into a stainless steel mold with dimensions of 13 cm $\times$ 15 cm $\times$ 1.6 cm. The as-cast plates were then fully solutionized using a two-step annealing schedule, at 385 °C for 12 h and at 430 °C for 30 h in an argon environment, to remove any precipitates. The casting and heat treatment procedures were developed by Dr. Xu through trial and error, specifically for these materials, in order to remove as much of the impurities as possible and to minimize any precipitates in the annealed plates. The absence of precipitates greater than 100 nm in the As-Cast materials was indicated with Scanning Electron Microscopy (SEM) and Energy Dispersive X-ray Spectroscopy (EDS). Note, the same materials were used in previous works [29,31].

The As-Cast plates were cut using Electric Discharge Machining (EDM) into bars and tiles having dimensions of 10 cm $\times$ 1.3 cm $\times$ 1.3 cm and 7.5 cm $\times$ 7.5 cm $\times$ 1.3 cm, respectively. The bars and tiles/plates were processed via ECAE using specialized tooling built by Shear Form, Inc. (Bryan, TX, USA) and equipped with a backpressure capability. For this study, all materials were processed through 4 passes via route B_C. The motivation for selecting this route is based on Segal's initial description of possible ECAE routes for both bar and plate geometries that maximize the amount of fully worked material in the extrudate billet [32,33]. Details of the processing steps have been described by Krywopusk et al. and Kecskes et al. [28,34].

Six sets of Mg alloy samples were fabricated for comparative testing. Because of the competition between grain refinement and precipitation within these alloys, two different ECAE processing conditions were explored, and the as-cast, fully solutionized Mg-9Al (9A) and Mg-6Al (6A) samples were compared to the samples produced through these two process conditions. In the first, hereafter referred to as "ISO", the material was extruded at 300 °C, and the same temperature was maintained through all four passes. In the second, hereafter referred to as "STEP", the material was extruded at 300 °C for the first pass, then at 250 °C for the next three passes. For both cases, the applied backpressure was adjusted to suppress shear localization in the extrudates. Between passes, gross surface defects were removed by grinding and machining. Maintaining a constant temperature was expected to allow the microstructure of the ISO samples to equilibrate as the bulk of the material became fully worked. It was expected that grain refinement would saturate at a minimum value, while the size of the precipitates would reach a maximum value. Both the grain sizes and the precipitates were expected to be finer for the STEP samples. Thus, the six microstructures that we studied were 6A & 9A As-cast, 6A & 9A ISO, and 6A & 9A STEP.

Several 3-mm rods were cut using EDM from each sample along three orthogonal directions relative to the extrusion direction. Each of these rods was then further sectioned into 3 mm $\times$ 200 µm specimen disks that were mechanically polished for the LDMF spall experiments. Prior to the spall experiments, the samples were characterized using SEM, EDS, and Electron Backscatter Diffraction (EBSD) analyses. The As-Cast samples had very large $\sim$500 µm grain sizes and were free of $\gamma - Mg_{17}Al_{12}$ precipitates with only trace levels of Fe-based impurity precipitates, detected above the resolution limit of the SEM. In contrast, an equivalent analysis revealed highly heterogeneous microstructures for all ECAE samples, consisting of regions containing fully recrystallized Mg grains interspersed with $\gamma - Mg_{17}Al_{12}$ precipitates. Typically, the recrystallized grain size was

about 2–3 µm, while the size of the precipitates were 0.5–1 µm. Details of the microstructure characterization processes are included in [35]. Occasionally, there were a few coarse, partially refined parent grains. The differences between the compositions were primarily reflected in the number of precipitates, with the Mg-9Al samples containing significantly more than the Mg-6Al samples. Within each composition, the ISO samples exhibited a more uniform microstructure with coarser precipitates than those observed in the STEP samples. Characteristic EBSD inverse pole figures and backscattered electron micrographs for 9A Step, 9A ISO, and 6A STEP are displayed in Figure 1 and show grain and precipitate sizes and distributions. The averaged grain size reported in this figure is based only on the fully recrystallized region. Furthermore, Table 1 provides a summary of all relevant microstructure length scales for all six sample sets.

Table 1. Average values for key microstructure length scales for all sample sets. There is no data to show for 6A ISO, but the length scales are expected to resemble 9A ISO.

Microstructures	Grain Size (µm)	Precipitate Size (nm)	Precipitate Spacing (nm)
6A As-Cast	~500	N/A	N/A
9A As-Cast	~500	N/A	N/A
6A ISO	–	–	–
9A ISO	2.58 ± 0.26	480 ± 29	1003 ± 17
6A STEP	2.71 ± 0.48	350 ± 16	807 ± 13
9A STEP	2.07 ± 0.22	410 ± 18	671 ± 15

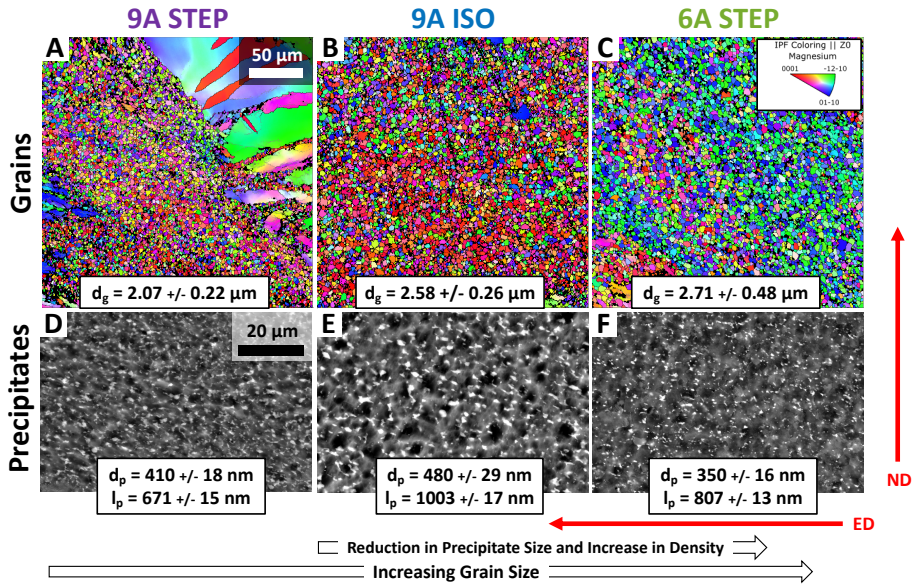


Figure 1. Microstructure characterization of the ECAE-processed samples. EBSD Inverse Pole Figures (IPFs) showing characteristic grain size, distribution, and orientation for (**A**) 9A STEP, (**B**) 9A ISO, and (**C**) 6A STEP. Backscattered electron micrographs showing the precipitate size and spacing for (**D**) 9A STEP, (**E**) 9A ISO, and (**F**) 6A STEP. The sample orientation is shown by the solid arrows in the lower right-hand corner to indicate the extrusion direction (ED) and normal direction (ND). (Figure reproduced with permission from [35]).

2.2. Laser-Driven Micro-Flyer Spall Experiments

The LDMF spall experiment achieves a plate impact event by using a high energy laser pulse to accelerate a small metal disk flyer towards a target; this concept is shown schematically in the center frame of Figure 2. The terms "flyer" and "impactor" are used interchangeably to refer to the accelerated disk. Upon impact, the spall response is determined through Photonic Doppler Velocimetry (PDV) measurements of the particle

velocity on the target's free surface. The primary challenges associated with this method are (1) maintaining a high degree of flyer and impact planarity, and (2) obtaining a consistent high-quality PDV return signal for spall calculations. This work is among the first to demonstrate the application of high-throughput LDMF experimental methods in the context of spall failure.

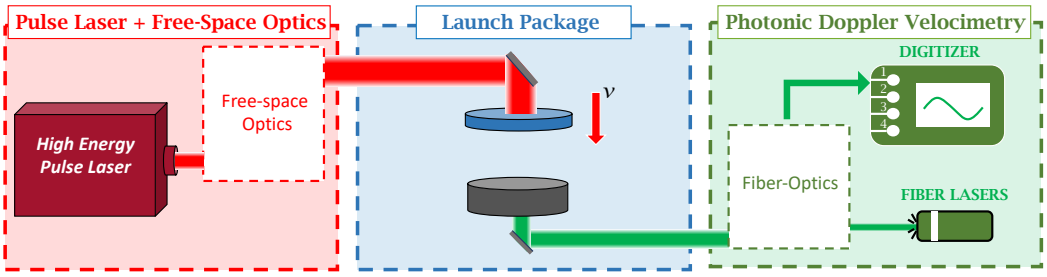


Figure 2. Schematic of Laser-Driven Micro-Flyer experiment. (**Left**) The pulse laser and free-space optics that prepare the laser pulse for optimal micro-flyer launch. (**Center**) The launch package depicting a simplified schematic view of the flyer-specimen impact. The flyer/specimen are not to scale, but typical thicknesses are ∼50–200 µm and diameters are ∼1–3 mm. (**Right**) A schematic of the PDV measurement system.

The LDMF experimental apparatus can be divided into three subsystems: (1) the pulse laser and free-space optics, (2) the launch package, and (3) the diagnostics (primarily, the PDV system). Figure 2 shows a schematic representation of our system based on these sections. The primary purpose of the pulse laser and free-space optics components, shown on the left in Figure 2, is to emit and shape a single high-energy pulse to accelerate a flyer disc with optimal planarity to a desired impact velocity. Our system uses a 1064-nm Nd:YAG 2.5 J 10-Hz 10-ns laser with a beam quality (M^2 value) of ∼15 (Spectra Physics Quanta-Ray Pro-350).

The second subsystem, the launch package, is designed to (1) facilitate optimal ablation conditions for planar flyer launch and (2) ensure reproducible planar impact at a well-defined impact velocity. The launch package is a layered composite consisting of three parts: a flyer stack, a spacer, and the specimen. The flyer stack is a glass-epoxy-foil laminar composite, where the foil is the flyer material. The laser is focused through the glass to ablate the epoxy layer; the hot expanding gases eject and accelerate the flyer. Besides serving as structural support for fixturing components in the experiment, the glass also confines the ablation products to optimize the energy conversion from the laser to the flyer's kinetic energy; conversion efficiencies are typically ∼30%. The flyers are precut from the foil using a femtosecond laser to further minimize launch-induced bending and maximize the impact area. The flyer planarity and velocity are calibrated independently prior to each set of experiments. A side profile view of the flyer is imaged using a high-speed camera to provide a measure of the planarity (Shimadzu HPV-X2).

In the third subsystem, our primary diagnostic is a heterodyne frequency-upshifted PDV system [19] focused on the free-surface of the specimen (or flyer when measuring impact velocities). The reference leg is frequency shifted by 2.3 GHz to better resolve low velocity signal and avoid signal overlap with unwanted power leakage. Note that the material response is averaged over the focused PDV spot size (∼80 µm diameter) and is sufficiently large relative to the microstructure length scales to adequately sample the material response.

The material and geometry of the launch package depend on the sample's material properties, microstructure, and anticipated spall characteristics. Here, Al flyers approximate the shock impedance of the Mg alloys, and both 50 µm and 100 µm Al flyers are fabricated from Hard AluFoil sheets. The flyer diameter is chosen to be 1.5 mm to maximize the impact area for probing the largest microstructure length scales. The specimens are ∼200 µm thick

disks with diameters of 3 mm, double-side polished with diamond lapping paper to a 1-µm mirror finish.

2.3. Spall Failure Analysis

The basic approach to analyzing plate impact experiments designed for spall failure has been summarized by [1]. The propagation and interaction of waves in the plate impact experiment (and therefore in our LDMF spall experiment) are shown in the Lagrangian time-distance plot of Figure 3A. Free-surface particle velocities are measured at the rear surface of the target using PDV as described earlier. An idealized free-surface velocity vs. time plot is shown in Figure 3B, based on the wave propagation diagram in Figure 3A.

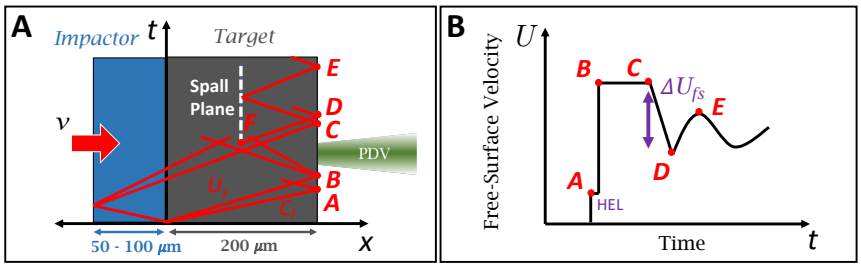


Figure 3. The spall failure process via plate impact. (**A**) A Lagrangian time vs. position diagram over the plate impact event depicting the propagation of waves leading to spall failure. (**B**) An idealized velocity vs. time trace gleaned from velocimetry measurements of the target's free-surface. The points on the curve follow those specified in (**A**).

Upon impact (t = 0, v = v), compression shock waves initiate and propagate into the impactor and the target. When the compression wave interacts with a free-surface, it reflects as a rarefaction fan; this occurs first at the impactor's free surface. Moreover, when the compression wave in the target reaches the target's free-surface, we observe a corresponding increase in velocity. We depict a two-wave structure (an elastic precursor followed by a plastic shock) propagating through the target in Figure 3B. The elastic precursor propagates at the longitudinal wave speed, C_L, followed shortly after by the plastic shock traveling at the shock speed U_S. The stress level corresponding to the velocity at point A represents the Hugoniot Elastic Limit (HEL), which defines the dynamic elastic limit of the material in the uniaxial strain condition. Depending on the target thickness, impact velocity, wave speeds, and PDV signal quality, the elastic precursor may not be observed.

The velocity at point B, U_B, corresponds to the maximum compression shock stress, Σ_S, in the material. This shock stress sustained by the target material is approximated by

$$\Sigma_S = \frac{1}{2}\rho_0 U_S U_B, \tag{1}$$

where ρ_0 is the initial material density and U_S is the shock speed. Here the properties of AZ31B Mg alloy were assumed for all samples; ρ is 1780 kg m^{-3} and U_S is estimated by assuming the linear equation of state from Marsh et al. [36] with a bulk wave speed, C_0, of 4540 m s^{-1} and a parameter, S_1, of 1.21.

After both compression waves reflect as rarefaction fans, they eventually meet and overlap within the target to create a region of high tensile stress; this position is referred to as the spall plane. If the stresses are sufficiently high, voids/cracks will nucleate and may grow and coalesce. The occurrence of spallation (the rapid creation of new surfaces on the interior of the target) results in the emission of a recompression wave (at point F in Figure 3A) that is seen as a reduction in velocity at point D. Following the arrival of the recompression wave at the target's free-surface, the wave continues to propagate and reflect between the target's free-surface and the newly created free-surfaces within the spall plane. This manifests as an oscillatory response in the velocity trace. The free-surface velocity at point D is a measure of the maximum tension and the drop in velocity ($\Delta U_{fs} = U_C - U_D$)

is referred to as the pullback velocity. ΔU_{fs} is used to determine the spall strength, Σ^*. The "uncorrected" spall strength is given by [1]

$$\Sigma^* = \frac{1}{2}\rho_0 C_0 \Delta U_{fs}. \quad (2)$$

We use the simplified "uncorrected" measure, denoted by the asterisk, as opposed to a corrected measure [1], because the spall strengths are low and our analysis is focused on relative trends in the data, as opposed to absolute spall strength values.

Lastly, the strain rate, $\dot{\epsilon}$, can be determined by estimating the velocity gradient between points C and D. This is given by

$$\dot{\epsilon} = \frac{1}{2C_0}\frac{\Delta U_{fs}}{|t_C - t_D|}, \quad (3)$$

where t_C and t_D are the times at points C and D in Figure 3B. These are all conventional definitions of these quantities in the spall literature.

3. Results and Discussion

A total of 678 spall experiments were performed across the six Mg alloy microstructures (recall that the six sample sets are 6A & 9A As-Cast, 6A & 9A ISO, and 6A & 9A STEP). This is the single largest collection of spall data to date on any material. For each microstructure, spall experiments were performed along 3 orthogonal directions with respect to the material orientations: "ED" and "ND" refer to impacts along the extrusion and normal directions for the As-Cast and ECAE processed samples, respectively; "LD" and "TD" refer to impacts along the longitudinal and transverse directions for all sample sets. The breakdown of the number of tests, N, per sample set and orientation, as well as the thickness mean, h_{mean}, and standard deviation, h_{std}, are reported in Table A1.

The LDMF experiments were carried out under the same conditions to ensure reliable sample-to-sample comparisons. All the ECAE processed samples, 6A ISO, 6A STEP, 9A ISO, and 9A STEP, were impacted with an impactor thickness, h_I, of 50 μm and the 6A & 9A As-Cast samples were impacted with h_I = 100 μm. Thicker plates were utilized in our effort to understand and reduce the experimental uncertainties associated with this method. Impact velocities were tailored so experiments attained similar mean Σ_S. The nominal impact velocities for the 50 μm and 100 μm thick flyers were 700–800 ms^{-1} and 550–600 ms^{-1}, respectively. For all experiments, the tensile strain rate $\dot{\epsilon}$ is $\sim \mathcal{O}(10^6)$ s^{-1}.

During our investigations, we found that 100 μm thick flyers provided significantly better consistency and control in the impact velocity, v. This is one factor that drives the reproducibility of Σ_S and its effect is shown in Figure 4. To ensure that the longer pulse duration does not affect the results for comparison purposes, we impacted a subset of 9A STEP samples in the same orientation with both 50 μm and 100 μm flyers and found no statistically significant differences in the results. The only difference observed was in the overall spread (or control) of Σ_S, as shown in Figure 4. The precise origin of the high spall strength variation for a given peak shock stress requires further investigations. The experimental observations in Figure 4 suggests that while some of this variation comes from experimental error, most likely it derives from variations in the 9A STEP sample microstructure.

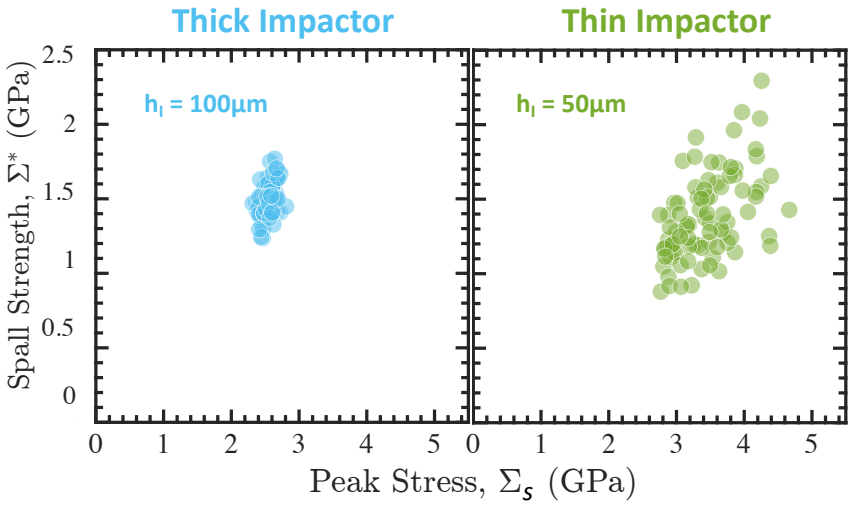


Figure 4. The influence of impactor thickness on the peak shock stress. Σ^* vs. Σ_S for (**left**) 6A As-Cast impacted with h_I = 100 µm and (**right**) 6A STEP impacted with h_I = 50 µm.

3.1. Spall Strength

ANOVA tests were performed to quantify the statistical differences in Σ^* as a function of impact orientation. The resulting box-plots are show in Figure 5. Considering first the effects of orientation within a given microstructure, no statistically significant differences were found in Σ^* based on orientation within a 95% confidence interval, with the exception of 9A STEP in Figure 5F. It is well-known from literature that the $4B_C$ ECAE processing route provides a mostly equiaxed sample microstructure with a weak crystallographic texture. That is, the sample behavior is expected to be quasi-isotropic. As such, only minimal variations in spall strength with orientation were expected. For the As-Cast samples, the orientation variation is minimal. For the ISO samples, the orientation variation is also minimal. In contrast, a greater orientation dependency is observable in the STEP samples, although it is not consistent with orientation between 6A and 9A. This dependency is likely accounted for by the change in extrusion temperature and its consequence on the evolution of the microstructure. That is, the lower processing temperature may lead to finer precipitates and greater overall non-uniformity of the microstructure which is reflected in a greater scatter in the spall strength data. The complete set of spall results is presented in Appendix A, where Table A2 summarizes the Σ^* means and standard deviations, and Figures A1 and A2 plot Σ^* vs. Σ_S for all six sample sets.

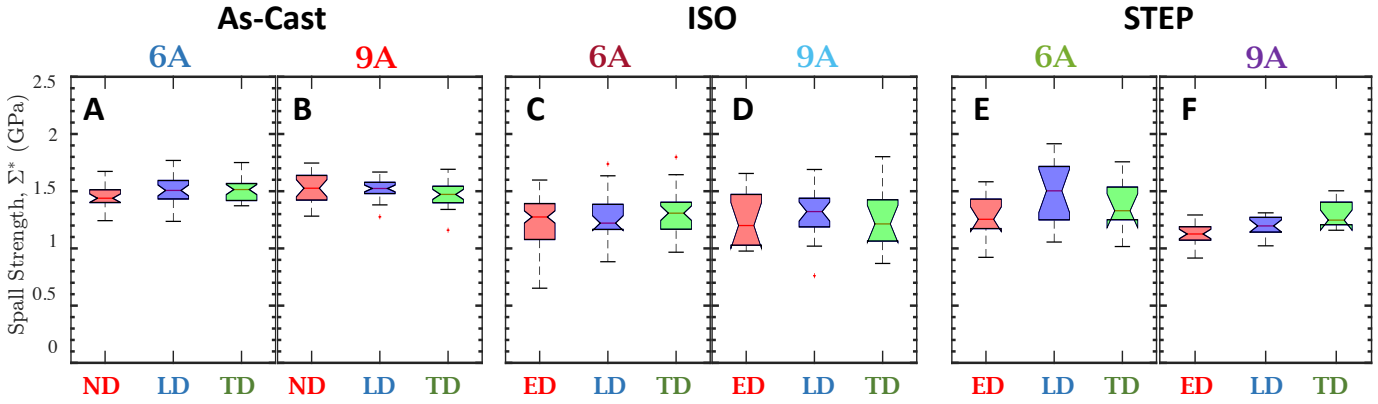


Figure 5. Orientation and sample-based spall strength statistical distributions. Orientation-based box-plots showing the relative distributions for the ND/ED, LD, and TD directions (left to right) for (**A**) 6A As-Cast, (**B**) 9A As-Cast, (**C**) 6A ISO, (**D**) 9A ISO, (**E**) 6A STEP, and (**F**) 9A STEP.

Informed by the orientation-dependent results, we now choose to consider each set as a single collective, independent of orientation (for 9A STEP, where anisotropy is most clearly exhibited, this simplifying assumption does not materially affect our subsequent observations). As seen in Figure 5, the 6A and 9A As-Cast are statistically indistinguishable and demonstrate the highest spall strength Σ^*. 6A STEP shows the next highest spall strength, followed by 6A and 9A ISO which show no statistically significant differences between them. Lastly, 9A STEP exhibits the lowest spall strength. The corresponding quantitative information is presented in Table A2.

The results for the As-Cast samples are as expected. In the absence of precipitates, the different solute levels do not affect the microstructure of the material, and the spall response of these coarse-grained materials (6A and 9A As-Cast) should not be significantly different according to current models. Considering the 6A and 9A ISO samples, these have similar and homogeneous microstructures, and correspondingly they have similar spall behavior. The similar and homogeneous microstructures may be attributable to the nature of the B_C rotations between passes. The $4B_C$ ECAE process generates a series of intersecting shear planes in the sample plate, which, in turn, generates a uniform distribution of precipitates in the bulk. After the first pass, existing precipitates would grow with successive passes, while new precipitates would nucleate alongside the dynamic recrystallization and grain refinement process. In contrast, for the 6A and 9A materials made by the ECAE STEP process, a more heterogeneous microstructure is expected and observed. While the sequence of the rotations is the same, the extrusion temperature is lower. This leads to a slower growth of new precipitates which would have a finer size distribution. Concurrently, the lower temperature also hinders grain refinement and the breakdown of parent grains. Such an unrefined parent grain is visible in Figure 1A. As such, a greater level of heterogeneity would be reflected in the STEP samples and their observed spall behavior. Finally, due to its lower Al content, there would be fewer precipitates in 6A ISO than in 9A ISO. This would hold true in the 6A and 9A STEP samples as well. Despite the general trends obtained from the averaged data sets, there is greater uncertainty and variability in the data which warrants a closer look at the reasons for the scatter in the ECAE processed samples.

Independent of composition, ECAE materials have much finer grain sizes than their As-Cast equivalents. The Mg-Al ECAE samples are no different, while also having precipitates. In combination with the finer grain sizes, this results in higher yield strengths [35]. However, as observed, they have lower spall strengths than the As-Cast materials. In the ISO samples, in contrast with the STEP samples, the constant and higher extrusion temperature is expected to lead to coarser grains and more uniformly distributed coarser precipitates. Conversely, the STEP samples are processed at a lower temperature for 3 passes, which may yield a finer distribution of precipitates, but without the same level of uniformity. Thus the observations of Figure 5 suggest that the spall behavior is more strongly affected by the presence of precipitates than by grain size.

The spall strength is also affected by the composition which, in turn, determines the number density and spacing of the precipitates. A key aspect of the data is that a lower density of fine precipitates may be more advantageous than a higher density (i.e., fewer void nucleation sites); this is clearly illustrated by the difference in spall strengths of the 6A and 9A STEP samples. However, a larger spacing of these sites may actually lead to greater variability in the next stages of the spallation process (void coalescence and subsequent fracture failure). That is, wider spacing of precipitates may lead to larger grains and more complicated fracture paths. The greater scatter in the data for 6A ISO and STEP samples compared to those of the 9A samples seems to indicate this.

3.2. Macroscopic Damage Morphology

Macroscopic optical images of the damage surface provide a more complete picture of the dynamic failure process within the LDMF experiments. The macroscopic damage morphology was examined for all six sample sets and for all three impact orientations in each case (note all

of these observations represent the post-mortem observations for loading over similar times). Only a subset of results are shown in the following figures, with a more comprehensive set in Appendix A in Figures A3 and A4. For each material, the damage morphology was not found to change substantially with shock stress over the small range of imposed shock stresses in these experiments. This is illustrated in Figure 6 with sample 9A ISO ED where similar macroscopic damage morphologies are visible across this shock stress range.

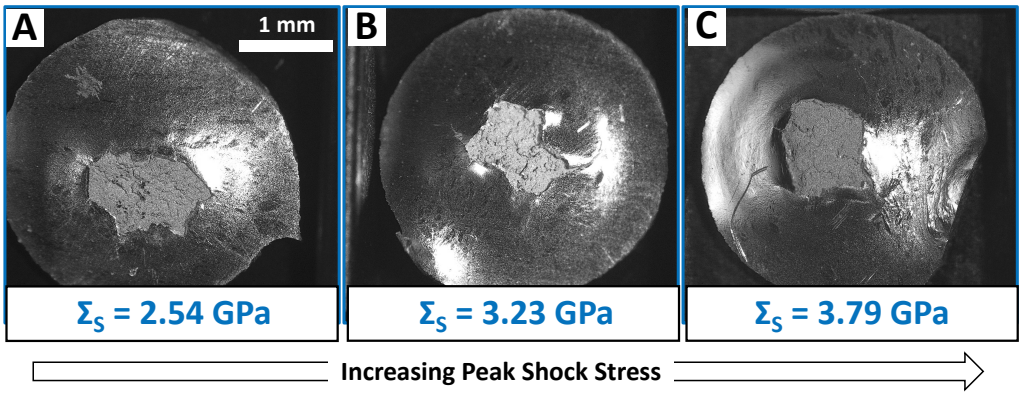


Figure 6. Macroscopic damage morphology with increasing Σ_S. Sample 9A ISO ED macroscopic free-surface spall damage at (**A**) low, (**B**) moderate, and (**C**) high Σ_S.

An interesting observation is that the macroscopic damage morphology changes with orientation even though the spall strength itself is insensitive to orientation (as shown in Section 3.1). These images are representative of the many tests performed in each orientation. For example, in the case of 9A ISO shown in Figure 7, while the spall strength distributions from Figure 5D show no statistically significant orientation dependency, the damage morphology does. The extrusion and transverse directions exhibit full spallation with the significant ejecta, whereas the longitudinal direction consists of only large area cracking with very limited fragmentation. Overall, 6A and 9A ISO samples show the clearest orientation-dependent damage morphologies. For 6A and 9A STEP, the trend is not sufficiently consistent to make any definitive statements. The As-Cast damage morphology is orientation-independent for both samples sets.

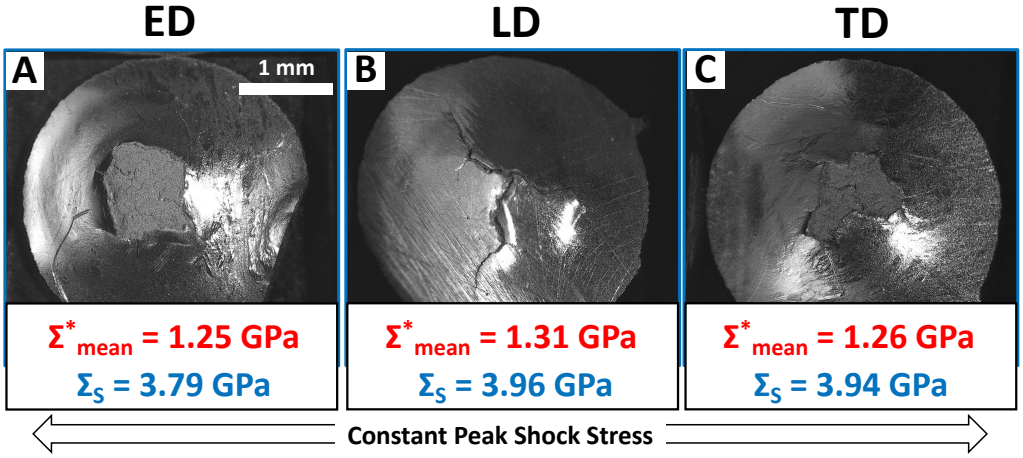


Figure 7. Orientation-dependent macroscopic damage morphology. Sample 9A ISO macroscopic free-surface spall damage in (**A**) ED, (**B**) LD, and (**C**) TD at nominally constant Σ_S.

The degree of macroscopic damage that is observed is consistent with the measured spall responses for each material sample set. The 6A and 9A As-Cast microstructures have the highest Σ^* and demonstrate the least damage with no visible fractures on the rear

surface. Samples 6A and 9A ISO, which show no statistically significant difference in Σ^*, have similar distributions of damage morphologies although having clear orientation dependencies. Sample 6A STEP, which shows the highest Σ^* of the ECAE-processed samples, also demonstrates a higher resistance to damage when compared to the ISO samples. Lastly, 9A STEP, which exhibits the lowest Σ^* demonstrates the most significant damage.

3.3. Microscopic Observations of Failure Surfaces

Guided by the macroscopic optical damage observations, we examined a subset of specimens from the ECAE-processed sample sets with high-resolution SEM, performing an assessment of the microscopic failure mechanisms. Since 6A and 9A ISO demonstrate statistically identical spall strengths and very similar macroscopic damage morphologies, we will omit 6A ISO from the discussion (for SEM images of 6A ISO fracture surfaces, please refer to Figure A5). Figure 8 depicts SEM micrographs from 9A STEP, 9A ISO, and 6A STEP (left to right) with both secondary electron (SE) and backscattered electron (BSE) detectors of the same region for each specimen. The BSE micrographs (bottom row) allow for the clearest view of the precipitates. In general, all imaged specimens depict ductile void growth failure. In the BSE micrographs, smaller equiaxed precipitates are observable and generally centered in the dimple cups. Interestingly, the specimens investigated show a homogeneous microstructure. This is in contrast to the pre-experimental microstructure characterizations from Figure 1 that showed far more heterogeneity, and suggest that the failure surfaces follow precipitate rich regions within the samples.

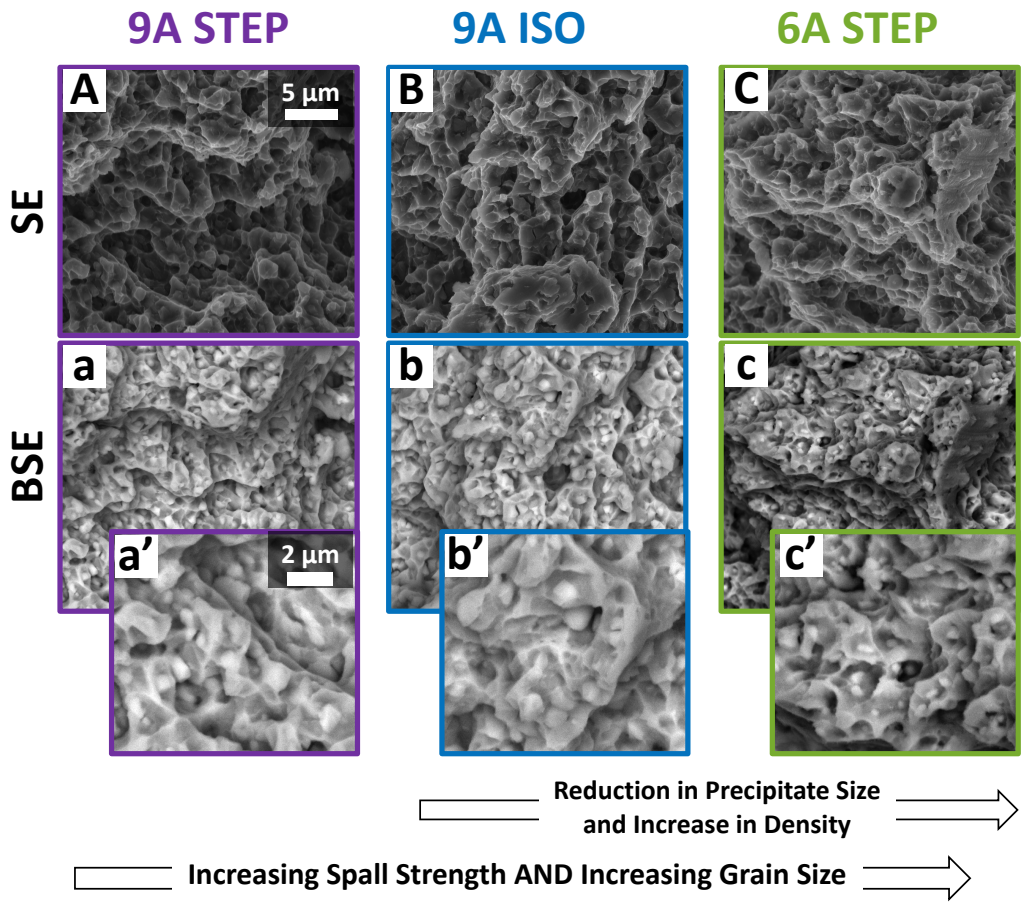


Figure 8. High-resolution SEM failure surface images of representative specimens from ECAE-processed sample sets. Each column depicts a specimen from a single sample set: (left) 9A STEP, (center) 9A ISO, and (right) 6A STEP. Micrographs are shown from (**A**–**C**) secondary electrons (SE), (**a**–**c**) backscattered electrons (BSE), and (**a′**–**c′**) magnified BSE. Frame (**A**) shows the scale bar for (**A**–**C**) and (**a**–**c**), and Frame (**a′**) shows the scale bar for (**a′**–**c′**).

While a more detailed microstructure analysis is required to make concrete conclusions, these preliminary observations provide some insight into the role of microstructure on the spall failure of these samples. For example, while the failure mode remains the same, the susceptibility to failure via void growth is exacerbated by the presence of an excessive number of non-uniformly dispersed precipitates in the 9A STEP sample. There is too much variability in the data with respect to orientation to draw further conclusions.

4. Summary

The LDMF experiments have allowed us to interrogate the role of certain aspects of the microstructure during the spall of Mg-Al alloys. One clear result is that even with a highly refined microstructure of 2–3 μm grains and small 0.5–1 μm equiaxed precipitates, the anticipated benefits of increased void growth resistance due to higher overall yield strength do not outweigh the detrimental effects of the increase in void nucleation sites. This is evident from the 8–19% reduction in spall strength from the As-Cast precipitate-free samples to the ECAE-processed samples. This strongly suggests that improved spall strength through precipitation strengthening may not be a viable path forward in this alloy system.

Across all samples examined via SEM, ductile void growth failure is observed with precipitates generally centered in ductile cups. Interestingly, relatively small changes in precipitate size (350–480 nm) and spacing (671–1003 nm) demonstrate a statistically significant influence on the spall strength (1.22–1.38 GPa) and variability (±0.17–0.29 GPa). Increased variability is specifically observed with an increase of non-uniformly distributed precipitates. This motivates a more comprehensive post-mortem microstructure analysis to better understand the subtle differences in void nucleation and growth.

These are among the first demonstrations of truly high-throughput spall characterization via the LDMF experimental technique. This large dataset over such a wide range of microstructures provides an important stepping-stone for improvement of these methods toward spall failure characterization and realizing the Materials-by-Design framework. Such efforts can provide important insights into the fundamentals of the spall failure process, and this may be valuable for the development of predictive models.

Author Contributions: C.S.D. refined the experimental method, performed the LDMF experiments, and wrote the manuscript. P.L. prepared LDMF samples, assisted with the LDMF experiments, and completed the post-mortem characterization of the samples. D.M. developed the experimental method and assisted with the analysis and writing of the manuscript. L.K. fabricated the ECAE samples, performed sample characterization, interpreted the results, and wrote parts of the manuscript. T.P.W. helped with defining the objectives of the materials processing effort and guided the experimental tasks to completion. K.T.R. helped with conceptualization of the effort, obtained funding resources, guided the project, helped interpret the results, and helped write the manuscript. All authors have read and agreed to the published version of the manuscript.

Funding: This research was sponsored by the U.S. Army Research Laboratory through the Materials in Extreme Dynamic Environments (MEDE) CRA and was accomplished under Cooperative Agreement Number W911NF-12-2-0022. The views and conclusions contained in this document are those of the authors and should not be interpreted as representing the official policies, either expressed or implied, of the Army Research Laboratory or the U.S. Government. The U.S. Government is authorized to reproduce and distribute reprints for government purposes notwithstanding any copyright notation herein.

Data Availability Statement: All of the data in this publication are publicly available at: https://craedl.org/pubs?p=6348&t=3&c=187&s=hemi&d=https:%2F%2Ffs.craedl.org#publications.

Acknowledgments: We thank Sean Lezcano and Nathaniel Davenport for their foundational work in developing the sample preparation and experimental methods. We thank Jenna Krynicki for helping to develop the sample surface preparation methodology. We thank Zhigang Xu at North Carolina A&T University for providing us with As-Cast Mg-Al sample materials. We thank Levi Johnson and David Gibbins for their assistance with ECAE experiments. We thank Chengyun Miao for his assistance in early-stage LDMF experiment development and analysis of results. We thank Justin

Moreno and Matt Shaeffer for their invaluable support with the development and operation of the laser shock facility.

Conflicts of Interest: The authors declare no conflict of interest.

Appendix A

Table A1. Sample population and thickness information. The orientation-specific and sample-specific total sample sizes and thickness means, h_{mean}, and standard deviations, h_{std}, for all of the experiments presented. All thickness measurements are expressed in units of μm.

Orientation		**6A As-Cast**			**6A ISO**			**6A STEP**	
	N	h_{mean}	h_{std}	N	h_{mean}	h_{std}	N	h_{mean}	h_{std}
ND/ED	22	216.8	±19.2	145	200.2	±15.7	29	196.5	± 5.6
LD	28	218.4	±2.7	65	194.5	±8.2	29	199.5	±4.7
TD	27	212.6	±5.6	66	180.1	±14.2	27	196.7	±7.2
ALL	77	215.9	±11.0	276	194.0	±16.3	85	197.6	±6.0
Orientation		**9A As-Cast**			**9A ISO**			**9A STEP**	
	N	h_{mean}	h_{std}	N	h_{mean}	h_{std}	N	h_{mean}	h_{std}
ND/ED	20	204.2	±13.1	32	208.5	±5.8	23	230.7	±4.1
LD	26	200.7	±5.2	29	205.6	±8.1	20	188.5	±4.7
TD	26	205.2	±5.1	29	207.7	±4.8	35	233.7	±5.2
ALL	72	203.3	±8.3	90	207.3	±6.4	78	221.2	±20.0

Table A2. Spall strength mean values and standard deviations. A summary of the orientation-specific and sample-specific Σ^* mean values and standard deviations. All values are expressed in units of GPa.

Orientation	**6A As-Cast**		**6A ISO**		**6A STEP**	
	Σ^*_{mean}	Σ^*_{std}	Σ^*_{mean}	Σ^*_{std}	Σ^*_{mean}	Σ^*_{std}
ND/ED	1.45	±0.10	1.22	±0.23	1.28	±0.19
LD	1.51	±0.12	1.26	±0.20	1.47	±0.27
TD	1.51	±0.10	1.30	±0.19	1.37	±0.22
ALL	1.49	±0.11	1.30	±0.22	1.38	±0.29
Orientation	**9A As-Cast**		**9A ISO**		**9A STEP**	
	Σ^*_{mean}	Σ^*_{std}	Σ^*_{mean}	Σ^*_{std}	Σ^*_{mean}	Σ^*_{std}
ND/ED	1.53	±0.12	1.25	±0.25	1.13	±0.09
LD	1.52	±0.09	1.31	±0.21	1.19	±0.09
TD	1.47	±0.11	1.26	±0.30	1.30	±0.12
ALL	1.50	±0.11	1.28	±0.24	1.22	±0.17

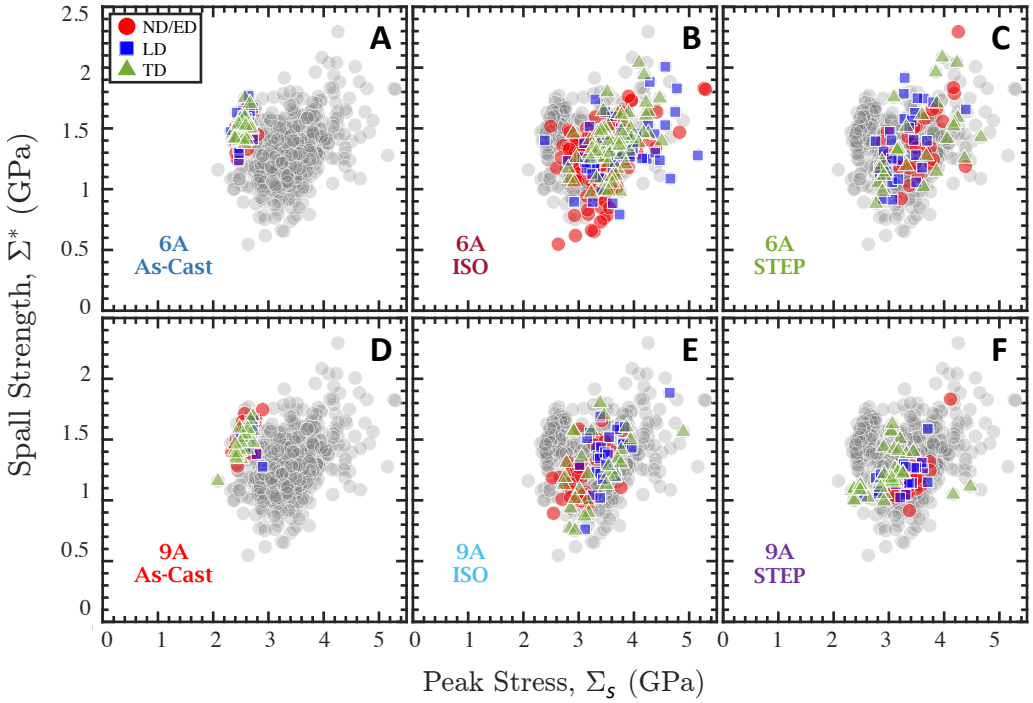


Figure A1. Orientation-based spall strength vs. peak shock stress results for all sample sets. Each frame compares orientation-based results for a specific sample set: (**A**) 6A As-Cast, (**B**) 6A ISO, (**C**) 6A STEP, (**D**) 9A As-Cast, (**E**) 9A ISO, and (**F**) 9A STEP. The full dataset is shown in the background in grey for direct comparison.

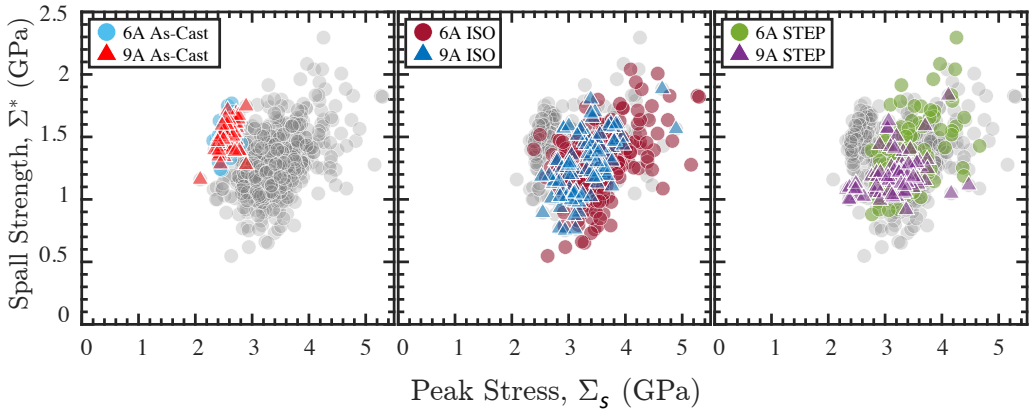


Figure A2. Spall strength vs. peak shock stress results for all sample sets. Each frame compares composition-based results for the same processing conditions: (**left**) As-Cast, (**center**) ISO, and (**right**) STEP. The full dataset is shown in the background in grey for direct comparison.

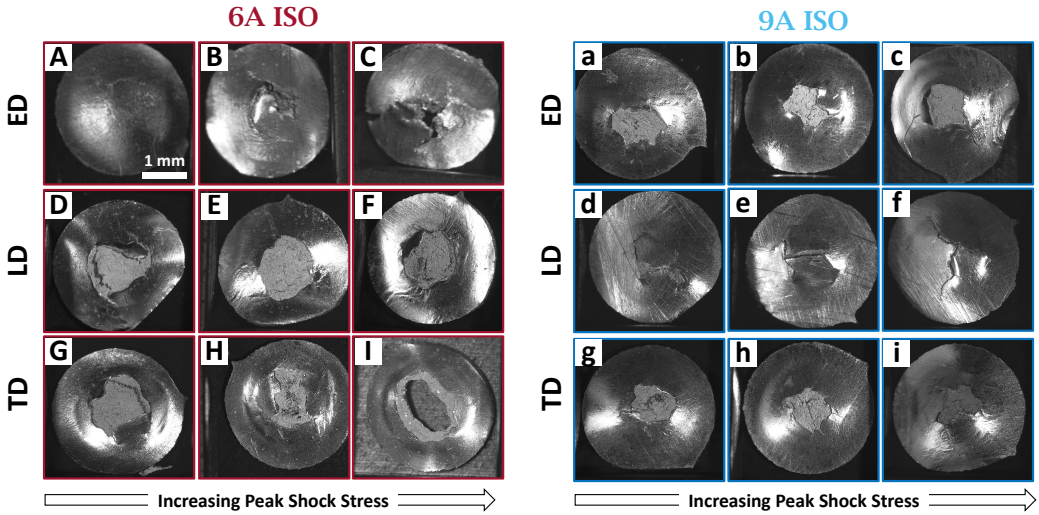


Figure A3. Macroscopic optical post-mortem images for ISO sample sets. Each 3 × 3 grid of images shows characteristic macroscopic damage morphologies for (**A**–**I**) 6A ISO and (**a**–**i**) 9A ISO. Each row shows the results for a specific impact orientation: (**top**) ED, (**middle**) LD, and (**bottom**) TD. The peak shock stress within each column is nominally identical and increases from left to right from low to mid to high based on the range shown in Figure A2.

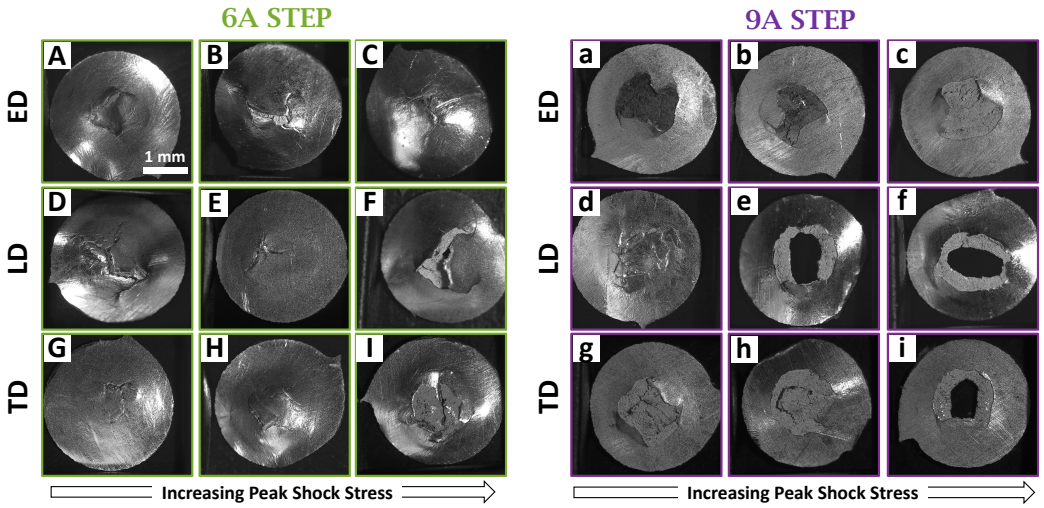


Figure A4. Macroscopic optical post-mortem images for STEP sample sets. Each 3 × 3 grid of images shows characteristic macroscopic damage morphologies for (**A**–**I**) 6A STEP and (**a**–**i**) 9A STEP. Each row shows the results for a specific impact orientation: (**top**) ED, (**middle**) LD, and (**bottom**) TD. The peak shock stress within each column is nominally identical and increases from left to right from low to mid to high based on the range shown in Figure A2.

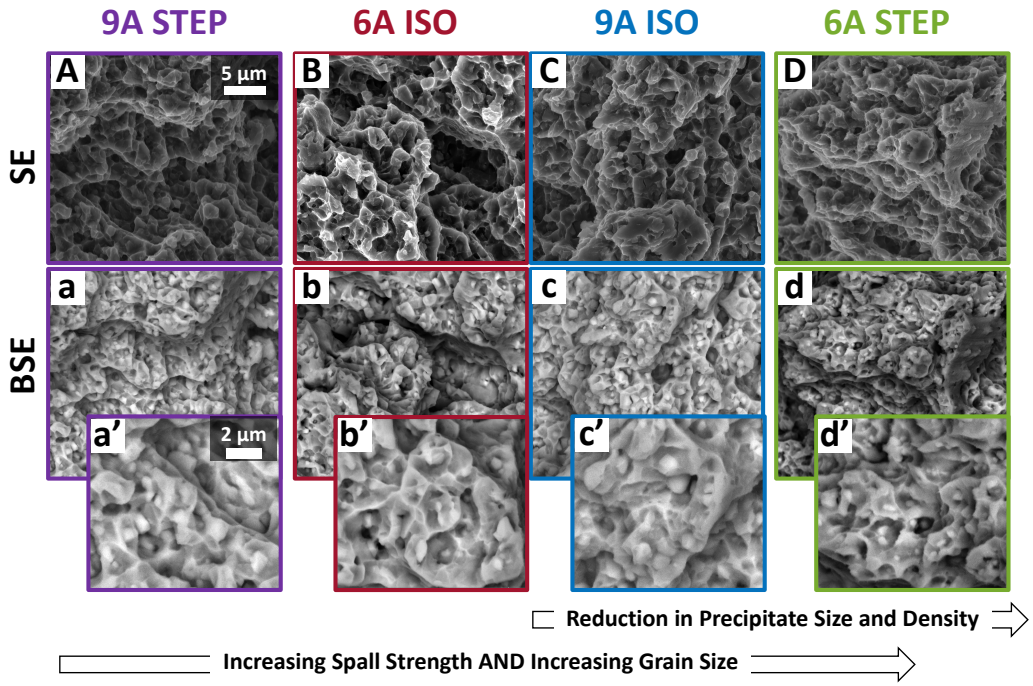


Figure A5. High-resolution SEM failure surface images of representative specimens from all ECAE-processed sample sets. Each column depicts a single sample set: (left) 9A STEP, (center-left) 6A ISO, (center-right) 9A ISO, and (right) 6A STEP. Micrographs are shown from (**A**–**D**) secondary electrons (SE), (**a**–**d**) backscattered electrons (BSE), and (**a′**–**d′**) magnified BSE. Frame (**A**) shows the scale bar for (**A**–**D**) and (**a**–**d**), and Frame (**a′**) shows the scale bar for (**a′**–**d′**).

References

1. Antoun, T.; Seaman, L.; Curran, D.R.; Kanel, G.I.; Razorenov, S.V.; Utkin, A.V. *Spall Fracture*; Springer Science & Business Media: Berlin/Heidelberg, Germany, 2003.
2. Meyers, M.A. *Dynamic Behavior of Materials*; John Wiley & Sons: Hoboken, NJ, USA, 1994.
3. Wu, X.; Ramesh, K.; Wright, T. The dynamic growth of a single void in a viscoplastic material under transient hydrostatic loading. *J. Mech. Phys. Solids* **2003**, *51*, 1–26. [CrossRef]
4. Molinari, A.; Wright, T. A physical model for nucleation and early growth of voids in ductile materials under dynamic loading. *J. Mech. Phys. Solids* **2005**, *53*, 1476–1504. [CrossRef]
5. Hazell, P.; Appleby-Thomas, G.; Wielewski, E.; Stennett, C.; Siviour, C. The influence of microstructure on the shock and spall behaviour of the magnesium alloy, Elektron 675. *Acta Mater.* **2012**, *60*, 6042–6050. [CrossRef]
6. Eswarappa Prameela, S.; Weihs, T.P. Deformation driven precipitation in binary magnesium alloys. In Proceedings of the Magnesium Technology, San Diego, CA, USA, 23–27 Febauary 2020; Springer: Berlin/Heidelberg, Germany, 2020; pp. 163–165.
7. Eswarappa Prameela, S.; Yi, P.; Liu, V.; Medeiros, B.; Kecskes, L.J.; Falk, M.L.; Weihs, T.P. Effect of second phase particle size on the recrystallized microstructure of Mg–Al alloys following ECAE processing. In Proceedings of the Magnesium Technology, San Diego, CA, USA, 23–27 Febauary 2020; Springer: Berlin/Heidelberg, Germany, 2020; pp. 167–173.
8. Ma, X.; Eswarappa-Prameela, S.; Krywopusk, N.; Kecskes, L.J.; Sano, T.; Weihs, T.P. Dynamic precipitation in a binary Mg-Al alloy during equal channel angular extrusion (ECAE). *Microsc. Microanal.* **2018**, *24*, 2222–2223. [CrossRef]
9. Prameela, S.E.; Yi, P.; Medeiros, B.; Liu, V.; Kecskes, L.J.; Falk, M.L.; Weihs, T.P. Deformation assisted nucleation of continuous nanoprecipitates in Mg–Al alloys. *Materialia* **2020**, *9*, 100583. [CrossRef]
10. Mallick, D.D.; Williams, C.; Wilkerson, J.W. A brief review of spall failure in pure and alloyed magnesium. *J. Dyn. Behav. Mater.* **2020**, *6*, 423–431. [CrossRef]
11. Mallick, D.D.; Prameela, S.E.; Ozturk, D.; Williams, C.L.; Kang, M.; Valentino, G.M.; Lloyd, J.T.; Wilkerson, J.W.; Weihs, T.P.; Ramesh, K.T. Spall strength in alloyed magnesium: A compendium of research efforts from the CMEDE 10-year effort. *Mech. Mater.* **2021**, *162*, 104065. [CrossRef]
12. Yu, X.; Li, T.; Li, L.; Liu, S.; Li, Y. Influence of initial texture on the shock property and spall behavior of magnesium alloy AZ31B. *Mater. Sci. Eng.* **2017**, *700*, 259–268. [CrossRef]
13. Garkushin, G.; Razorenov, S.; Krasnoveikin, V.; Kozulin, A.; Skripnyak, V. Effect of structural factors on mechanical properties of the magnesium alloy Ma2-1 under quasi-static and high strain rate deformation conditions. *Phys. Solid State* **2015**, *57*, 337–343. [CrossRef]

14. Farbaniec, L.; Williams, C.L.; Kecskes, L.; Ramesh, K.T.; Becker, R. Microstructural effects on the spall properties of ECAE-processed AZ31B magnesium alloy. *Int. J. Impact Eng.* **2016**, *98*, 34–41. [CrossRef]
15. Kanel, G.; Garkushin, G.; Savinykh, A.; Razorenov, S.; De Resseguier, T.; Proud, W.; Tyutin, M. Shock response of magnesium single crystals at normal and elevated temperatures. *J. Appl. Phys.* **2014**, *116*, 143504. [CrossRef]
16. Paisley, D.L.; Warnes, R.H.; Kopp, R.A. Laser-Driven Flat Plate Impacts to 100 GPa with Sub-Nanosecond Pulse Duration and Resolution for Material Property Studies. In Proceedings of the APS 1991 Topical Conference on Shock Compression of Condensed Matter, Williamsburg, VA, USA, June 17–20. 1991; Technical Report; Los Alamos National Lab: Los Alamos, NM, USA, 1991.
17. Paisley, D.L.; Luo, S.N.; Swift, D.C.; Greenfield, S.; Loomis, E.; Johnson, R.; Peralta, P.; Koskelo, A.; Tonks, D. Experimental method for laser-driven flyer plates for 1-D shocks. In Proceedings of the AIP Conference Proceedings, Waikoloa, HI, USA, 24–29 June 2007; American Institute of Physics: College Park, MD, USA, 2007; Volume 955, pp. 1337–1340.
18. Brown, K.E.; Shaw, W.L.; Zheng, X.; Dlott, D.D. Simplified laser-driven flyer plates for shock compression science. *Rev. Sci. Instruments* **2012**, *83*, 103901. [CrossRef]
19. Mallick, D.D.; Zhao, M.; Parker, J.; Kannan, V.; Bosworth, B.T.; Sagapuram, D.; Foster, M.A.; Ramesh, K.T. Laser-driven flyers and nanosecond-resolved velocimetry for spall studies in thin metal foils. *Exp. Mech.* **2019**, *59*, 611–628. [CrossRef]
20. Li, F.; Dlott, D.D. High throughput tabletop shock techniques and measurements. *J. Appl. Phys.* **2022**, *131*, 075901. [CrossRef]
21. De Rességuier, T.; Hemery, S.; Lescoute, E.; Villechaise, P.; Kanel, G.; Razorenov, S. Spall fracture and twinning in laser shock-loaded single-crystal magnesium. *J. Appl. Phys.* **2017**, *121*, 165104. [CrossRef]
22. Jones, T.L.; DeLorme, R.D.; Burkins, M.S.; Gooch, W.A. *Ballistic Evaluation of Magnesium Alloy AZ31B*; Technical Report; Army Research Lab: Aberdeen Proving Ground, MD, USA, 2007.
23. Rahmatabadi, D.; Pahlavani, M.; Marzbanrad, J.; Hashemi, R.; Bayati, A. Manufacturing of three-layered sandwich composite of AA1050/LZ91/AA1050 using cold roll bonding process. *Proc. Inst. Mech. Eng. Part J. Eng. Manuf.* **2021**, *235*, 1363–1372. [CrossRef]
24. Nitol, M.S.; Adibi, S.; Barrett, C.D.; Wilkerson, J.W. Solid solution softening in dislocation-starved Mg–Al alloys. *Mech. Mater.* **2020**, *150*, 103588. [CrossRef]
25. Wilkerson, J.W.; Ramesh, K.T. Unraveling the anomalous grain size dependence of cavitation. *Phys. Rev. Lett.* **2016**, *117*, 215503. [CrossRef]
26. Farbaniec, L.; Williams, C.L.; Kecskes, L.J.; Becker, R.; Ramesh, K.T. Spall response and failure mechanisms associated with a hot-extruded AMX602 Mg alloy. *Mater. Sci. Eng.* **2017**, *707*, 725–731. [CrossRef]
27. Williams, C.L.; Farbaniec, L.; Kecskes, L.; Bradley, J. Microstructural effects on the spall properties of ECAE and SWAP magnesium alloys: AZ31B-4E and AMX602. In *Proceedings of the AIP Conference Proceedings*; AIP Publishing LLC: College Park, MD, USA, 2017; Volume 1793, p. 100011.
28. Krywopusk, N.M.; Williams, C.L.; Kecskes, L.J.; Weihs, T.P. Characterization of spalled AZ31B processed by ECAE. *Mater. Sci. Eng.* **2019**, *767*, 138298. [CrossRef]
29. Prameela, S.E.; Yi, P.; Hollenweger, Y.; Liu, B.; Chen, J.; Kecskes, L.; Kochmann, D.M.; Falk, M.L.; Weihs, T.P. Strengthening magnesium by design: Integrating alloying and dynamic processing. *Mech. Mater.* **2022**, *167*, 104203. [CrossRef]
30. Nguyen, T.; Pipatpongsa, T.; Kitaoka, T.; Ohtsu, H. Stress distribution in conical sand heaps at incipient failure under active and passive conditions. *Int. J. Solids Struct.* **2019**, *168*, 1–12. [CrossRef]
31. Ma, X.; Prameela, S.E.; Yi, P.; Fernandez, M.; Krywopusk, N.M.; Kecskes, L.J.; Sano, T.; Falk, M.L.; Weihs, T.P. Dynamic precipitation and recrystallization in Mg-9wt.% Al during equal-channel angular extrusion: A comparative study to conventional aging. *Acta Mater.* **2019**, *172*, 185–199. [CrossRef]
32. Segal, V.M. Materials processing by simple shear. *Mater. Sci. Eng.* **1995**, *197*, 157–164. [CrossRef]
33. Segal, V.M. Equal channel angular extrusion of flat products. *Mater. Sci. Eng.* **2008**, *476*, 178–185. [CrossRef]
34. Kecskes, L.J.; Krywopusk, N.M.; Hollenweger, Y.; Krynicki, J.N.; Prameela, S.E.; Yi, P.; Liu, B.; Falk, M.L.; Kochmann, D.M.; Weihs, T.P. Recrystallization mechanisms, grain refinement, and texture evolution during ECAE processing of Mg and its alloys. *Mech. Mater.* **2021**, *162*, 104067. [CrossRef]
35. Sun, X.; Wu, D.Y.; Kang, M.; Ramesh, K.T.; Kecskes, L.J. Properties and hardening behavior of equal channel angular extrusion processed Mg-Al binary alloys. *Mater. Charact.* **2023**, *195*, 112514. [CrossRef]
36. Marsh, S.P. *LASL Shock Hugoniot Data*; University of California Press: Oakland, CA, USA, 1980.

Disclaimer/Publisher's Note: The statements, opinions and data contained in all publications are solely those of the individual author(s) and contributor(s) and not of MDPI and/or the editor(s). MDPI and/or the editor(s) disclaim responsibility for any injury to people or property resulting from any ideas, methods, instructions or products referred to in the content.